Journal of Manufacturing Processes 64 (2021) 276–284

Contents lists available at ScienceDirect

Journal of Manufacturing Processes

journal homepage: www.elsevier.com/locate/manpro

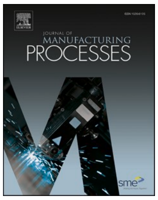

Technical Paper

Enhanced wettability in ultrasonic-assisted soldering to glass substrates

Caleb Wilson, Lonny Thompson, Hongseok Choi, Joshua B. Bostwick *

Department of Mechanical Engineering, Clemson University, Clemson, SC 29634, United States

ARTICLE INFO

Keywords:
Soldering
Ultrasonics
Wettability
Automation

ABSTRACT

Ultrasonic-assisted soldering (UAS) creates an enhanced metal-to-glass bond that is linked to the increased wettability of the solder line. Precision experiments are performed using an automated UAS system, with precise control over a large number of experimental parameters, to investigate the wetting properties of solder to glass. Results show that wettability is increased with (i) increasing ultrasonic power and (ii) decreasing solder tip height above substrate, both of which are linked to the acoustic radiation pressure delivered by the vibrating solder tip to the liquid solder melt. Surface tension forces dominate the mechanics and a capillary shape equation is derived that includes the effect of acoustic radiation pressure. Numerical solutions to the capillary shape equation compare well with experimental observations, suggesting the solder bead geometry can be predicted a priori from the model.

1. Introduction

Soldering is a commonly used means to join two non-ferrous metals together, such as bonding copper wires or electrical components to circuit boards. It is well-known that oxide layers develop on metallic substrates and affect the strength of the solder bond [1,2]. Flux is typically used in order to remove the oxide layer from the base metal through a redox chemical reaction, improve the wettability and adhesion of the solder, and prevent any further oxides from forming so that the solder can adhere directly to the exposed metal [3,4]. Unfortunately, this chemical reaction can release hazardous chemicals and cause health issues [5–7]. Additionally, any remaining flux residue can degrade electrical resistance and reduce the strength of the solder bond [8–10]. Ultrasonic assisted soldering (UAS) was developed as an alternative soldering method which eliminates the need for flux. The ultrasonic vibrations facilitate adhesion by removing the oxide layer through cavitation [11–13].

Cavitation is the formation and subsequent collapse of bubbles in rapidly changing pressure fields. In the case of UAS, the pressure differences in the molten solder arise from sound waves passing through the liquid as a series of compression and expansion waves. If an expansion wave is intense enough, it can create a pressure region lower than the vapor pressure of the liquid solder and cause a cavity to form from a microscopic nuclei within the solder melt [14]. The bubble oscillates with the changing pressure field and can grow in resonance with the sound field until it reaches a critical size where it can no longer efficiently absorb energy and it violently collapses during the next compression wave [15]. The collapsing bubble releases high levels of energy, temperature, and pressure, causing acoustic streaming and micro-jets [16,17]. The micro-jets impact the substrate's surface and break up the oxide layer to reveal fresh metal for effective bonding [13].

UAS has received much recent interest, primarily to join dissimilar materials [18–22]. For example, aluminum was rarely used as a solder base metal because it required a highly corrosive flux to remove its oxide [3,23]. However, with UAS, aluminum, ceramics, silica, glass, metal matrix composites, and other difficult-to-join materials have been successfully used in soldering applications [16,24,25]. Various manufacturing industries have implemented UAS in different areas that require unconventional soldering, such as solar panels for photovoltaics [26,27], joining of aluminum components to save weight and costs [28,29], and hermetic sealing [30]. While the ability to solder dissimilar materials has increased usage in UAS, the mechanisms of enhanced wetting and adhesion to ceramics is not as well understood as it was with metals. For example, in traditional soldering cavitation induced by ultrasonic vibrations removes the oxide layer so that solder can effectively bond to the metal substrate [31,17]. However, ceramics, especially glass substrates, are oxides, so cavitation cannot simply remove an oxide layer. It is speculated that the enhanced bonding in UAS to glass is related to (i) improved wettability and (ii) surface chemistry through the formation of covalent bonds between the ceramic substrate and metallic solder [32,33]. Our interest is in understanding solder wettability on glass substrates in the UAS process, as this is of critical interest to many precision manufacturing applications.

The experiments described in this paper are performed using a novel

---

* Corresponding author.

https://doi.org/10.1016/j.jmapro.2021.01.030
Received 17 October 2020; Received in revised form 18 January 2021; Accepted 18 January 2021
Available online 1 February 2021
1526-6125/© 2021 The Society of Manufacturing Engineers. Published by Elsevier Ltd. All rights reserved.

automated UAS system described by Shaffer et al. [34]. The system is built upon a 3D printer platform and has precision control over the motion of the solder tip, solder tip temperature, substrate temperature, solder feed rate, and ultrasonic energy, which makes it uniquely designed for our precision experiments in wetting on glass substrates. In UAS, the mechanism for enhanced wettability is acoustic radiation pressure, which is affected by both the (i) ultrasonic power and (ii) solder tip height above the substrate. We have performed a set of experiments to systematically investigate the role of each of these parameters on the solder wettability.

Intimately related to wettability is the adhesive strength of the solder-to-glass bond. In particular, the adhesive strength of the bond can be directly tied to its wetting properties through the work of adhesion [35],

$$W = \sigma(1 + cos\alpha), \tag{1}$$

which is the "reversible thermodynamic work required to separate the interface from the equilibrium state of two phases to a separation distance of infinity" [36]. Here σ is the surface tension of the liquid-gas interface and α is the static contact angle of the liquid-solid-gas system. Note that improved wettability corresponds to a decreased contact angle, which leads to increased work of adhesion of the solder bond. Therefore, our study of wettability could also lend itself to a better understanding of the enhanced adhesion shown in UAS process.

Surface tension is typically the dominant force which determines the shape of the solder bead, as determined by the Young-Laplace equation which relates the difference in pressures across an interface endowed with surface tension [37]. For the UAS process, the pressure is a sum of the internal liquid pressure and the acoustic radiation pressure applied by the oscillating tip [38]. We develop a theoretical model for the cross sectional shape of the solder line to compare with experimental observations. The acoustic radiation pressure on the solder bead inferred by measuring the amplitude of solder tip vibration will be used to predict the degree of wetting in the UAS process. This study can pave the way for wider use to the manufacturing industry which often seeks to develop precision soldering systems, where predicting the wetted width of a solder bead is important.

Verification of the extruded solder volume is important for repeatability in any manufacturing process and we have shown that our automated UAS system has the ability to lay down solder lines with constant cross-sectional area. However, the geometry of these solder lines varies greatly with the (i) substrate properties and (ii) ultrasonic power. Therefore, it is critically important to precisely understand the solder wettability in UAS, especially in light of the miniaturization of, e.g., electronics and heat sinks, where soldering must be performed in small spaces. Our focus is on glass substrates which is relevant to touch screen displays, but could also be extended to ceramic substrates, such as quartz or sapphire which are used in sensors and the packaging of electronics, or the thermally conductive ceramics used in high-power LEDs. Another advantage of UAS is low melt temperatures 140–185 °C which is important so as to not destroy components in circuit boards and more broadly reduces the residual thermal stresses associated with bonding materials with different thermal coefficients of expansion. In short, this study can be used to further develop means for bonding optical devices or components together or to substrates which provide superior stability and long term performance under prolonged exposure to environmentally adverse conditions in numerous applications, especially in defense and aerospace.

We begin this paper by describing the automated UAS system that we use to perform a set of experiments that focus on solder-to-glass wetting properties, as it depends upon (i) the ultrasonic power and (ii) the solder tip height, and the imaging techniques used to define the width, height, cross-sectional area, and contact-angle of the solder bead. Experimental results are then reported, in which we quantify the enhanced wettability due to increased ultrasonic power and decreased tip height. In the process, we show our automated system is capable of controlling the extruded solder volume to a high degree of accuracy. A model is then developed for the cross-sectional shape of the solder line due to acoustic radiation pressure. The resulting nonlinear differential equation is solved numerically and we show our model predictions compare favorably to experimental observations. Lastly, we offer some concluding remarks about the relevance of our study and future directions.

2. Experimental method

The automated UAS system described by Shaffer et al. [34] is schematically illustrated in Fig. 1(a) and is used to avoid human error associated with hand-held soldering and improve repeatability. The UAS system was built on the base of a Hyrel Hydra 340 FDM 3D printer, which provides control over various soldering parameters, such as solder tip motion, substrate heating, solder tip heating, solder extrusion rate, and ultrasonic power. Fig. 1(b, c) contrasts two solder lines with and without ultrasonication from our automated system. The difference is striking and it is clear that ultrasonic action leads to enhanced solder wettability, as shown by the increase in the wetted width of the solder line. The tip height and ultrasonic power have been selected as processing parameters for this study, as these parameters are most relevant to the acoustic radiation pressure delivered to the solder line [39]. The gantry and lift systems of the Hydra 340 allow accurate positioning and control of the solder tip along the X-, Y-, and Z-axes. The ultrasonic power is controlled by aSunbonder electronic unit that delivers a fixed electrical power to the PZT transducer that results in ultrasonic vibrations of the solder tip. The acoustic radiation pressure was inferred by measuring the amplitude of tip vibration as it depends upon the electric power. This will be discussed in detail when the theoretical model is compared to experimental observation.

Glass microscope slides (AmScope), i.e. borosilicate glass, are used as the substrate and cleaned in sequential steps with acetone, isopropyl alcohol, and deionized water in an ultrasonic bath to remove organic and inorganic contamination [34]. The solder used in experiments is S-Bond 140 M1 (S-Bond Technologies), which is an active tin-bismuth-titanium (Sn-Bi) based solder with a modified eutectic point. It is referred to as an 'active' solder because it contains low percentages of rare-earth, like Ce, highly reactive metals, like Ga and Ti, that activate bonding to oxide substrates in conjunction with mechanical activation [33]. These active rare earth metals are only about 0.35 wt.% weight of the solder while the tin and bismuth make up about 47 wt.% and 53 wt.%, respectively. Despite the low percentage of rare earth, Ti, and Ga additions, the active materials are able to effectively facilitate adhesion to the silica glass microscope slides which is not possible with some other types of solder.

Two sets of experiments were designed to investigate the role of acoustic radiation pressure which involve varying the (i) ultrasonic power and (ii) tip height. All other experimental parameters were held constant; the tip speed was set to 180 mm/min, the cross-sectional area to 0.2 mm^2, the length of the solder line to 70 mm, the solder tip temperature to 185 ± 2.5 °C, and substrate temperature to 195 ± 5 °C. For the experiments that vary the ultrasonic power, the tip height was set to 0.2 mm and the power ranged from 0 W to 5 W. For experiments with various tip heights, the power was set to 4.5 W and the tip height ranged from 0.1 mm to 0.6 mm. For each set of experimental parameters, 10 individual solder lines were prepared to analyze the wetting properties. Fig. 2 defines the cross-sectional geometry of the solder bead through the area A, wetted width W, height H, and contact-angle α, which describe the wetting properties.

The solder line profile was measured using an optical profiler (Olympus LEXT) consisting of a laser confocal microscope capable of measuring shape and surface roughness with X- and Y-resolutions of 120 nm, and Z-resolution of 10 nm. A typical cross-section scan is shown in Fig. 3(a) and a three-dimensional rendering of the full solder line is

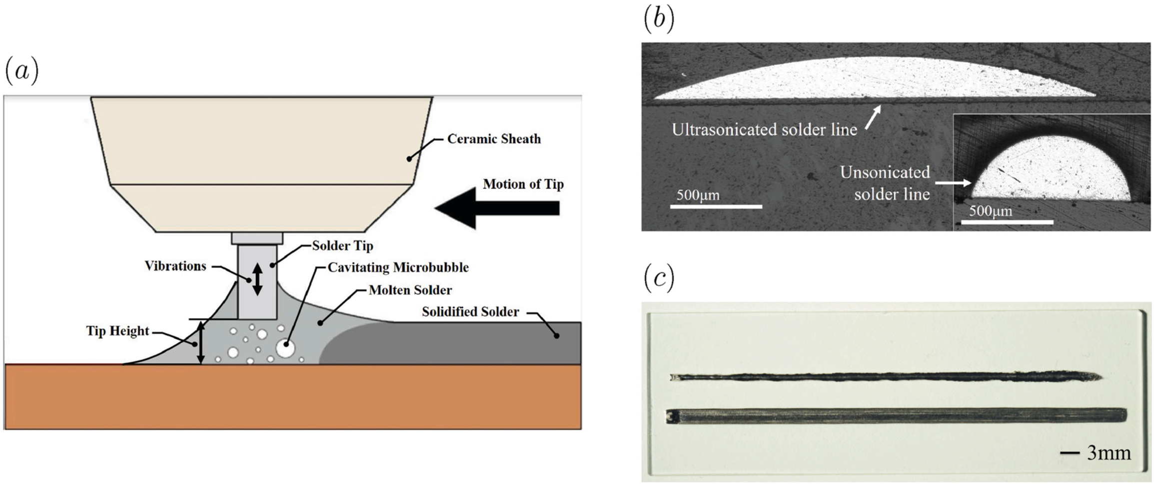

Fig. 1. (a) Experimental schematic of the UAS process with (b, c) contrasting sonicated and unsonicated solder lines in (b) cross-sectional and (c) top views.

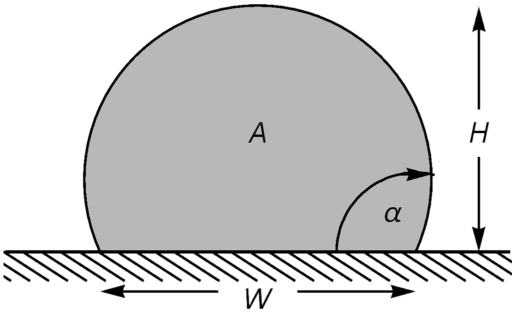

Fig. 2. Definition sketch for the cross-sectional geometry of the solder line.

shown in Fig. 3(b). For each cross section, the height H and width W of the solder line are calculated from the optical profiler data, while the cross-sectional area A and contact-angle α are computed via data processing in MATLAB. The average value of these parameters over 1000 cross sections has been taken along the length of the solder line. Each data point corresponds to the average of at least 10 individual solder lines with error bars corresponding to 95% confidence intervals.

3. Experimental results

Fig. 4(a) plots the width W [mm] against the applied ultrasonic power, which shows a steady increase in the width between 0 W to 2 W that plateaus near $W = 2.45$ mm for powers greater than 2 W. The plateau could be due to the equilibration of the acoustic radiation pressure with the wetting force at this particular contact angle $\alpha \approx 12^\circ$. The height H [mm] decreases with increasing power to maintain a constant cross-sectional area A [mm^2], as shown in Fig. 4(b). The height approaches a constant value $H \approx 0.13$ mm, even for low powers, suggesting this is a geometric effect. Fig. 4(c) plots the cross-sectional area A against power verifying that the automated UAS system delivers a constant cross-sectional area $A \approx 0.2$ mm^2. The exception is for 0 W, or no ultrasonic power is supplied, in which case the solder often fails to adhere to the surface, can get dragged by the tip, or is subject to wavy instabilities along its length associated with Plateau-Rayleigh breakup [40,41]. This observation of constant cross-sectional area will be used to derive a model for predicting the shape of the solder line. Fig. 4(d) plots the contact angle against power and is shown to decrease with increasing power and plateaus near $\alpha \approx 12^\circ$. The decrease in contact-angle leads to an increase in the work of adhesion, Eq. (1), and can potentially explain the enhanced adhesive bond due to UAS.

For the set of experiments for the role of tip height, the power of 4.5 W was used, which is typical value used for the UAS process. Fig. 5 (a) shows the width decrease with increasing tip height. This could be expected as the source of acoustic radiation pressure is farther from the substrate where wetting occurs, i.e. the acoustic intensity decreases. Increasing solder height is observed with increased tip height (cf. Fig. 5 (b)). Fig. 5(c) shows that the cross-sectional area has more variability from the target value 0.2 mm^2 than in the experiments with various ultrasonic powers. This could be due to a number of factors, including slightly different heat transfer conditions as the solder is melted from the combined heating of the solder tip and substrate. It is also worth noting

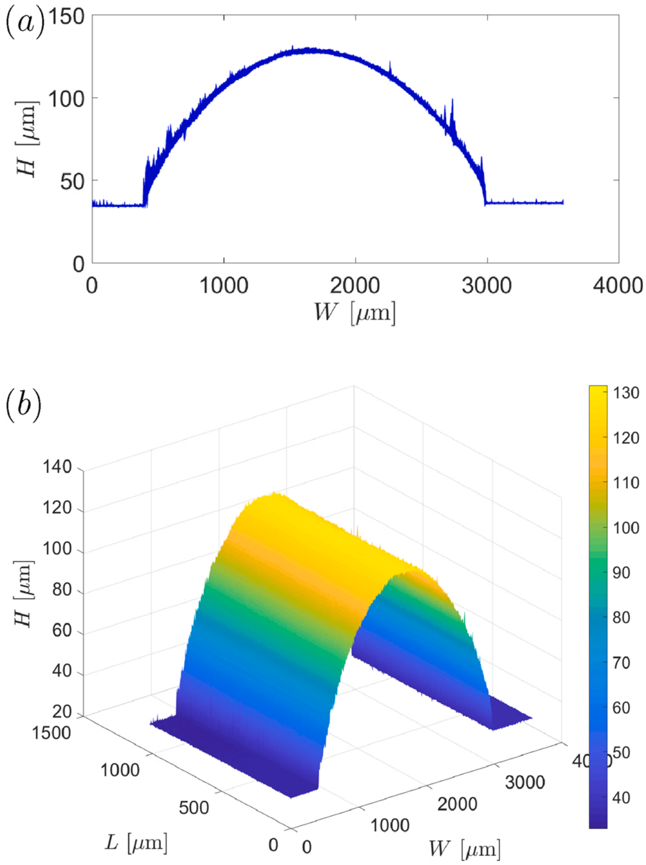

Fig. 3. Typical optical profile measurement of a solder line in (a) cross-sectional and (b) three-dimensional views.

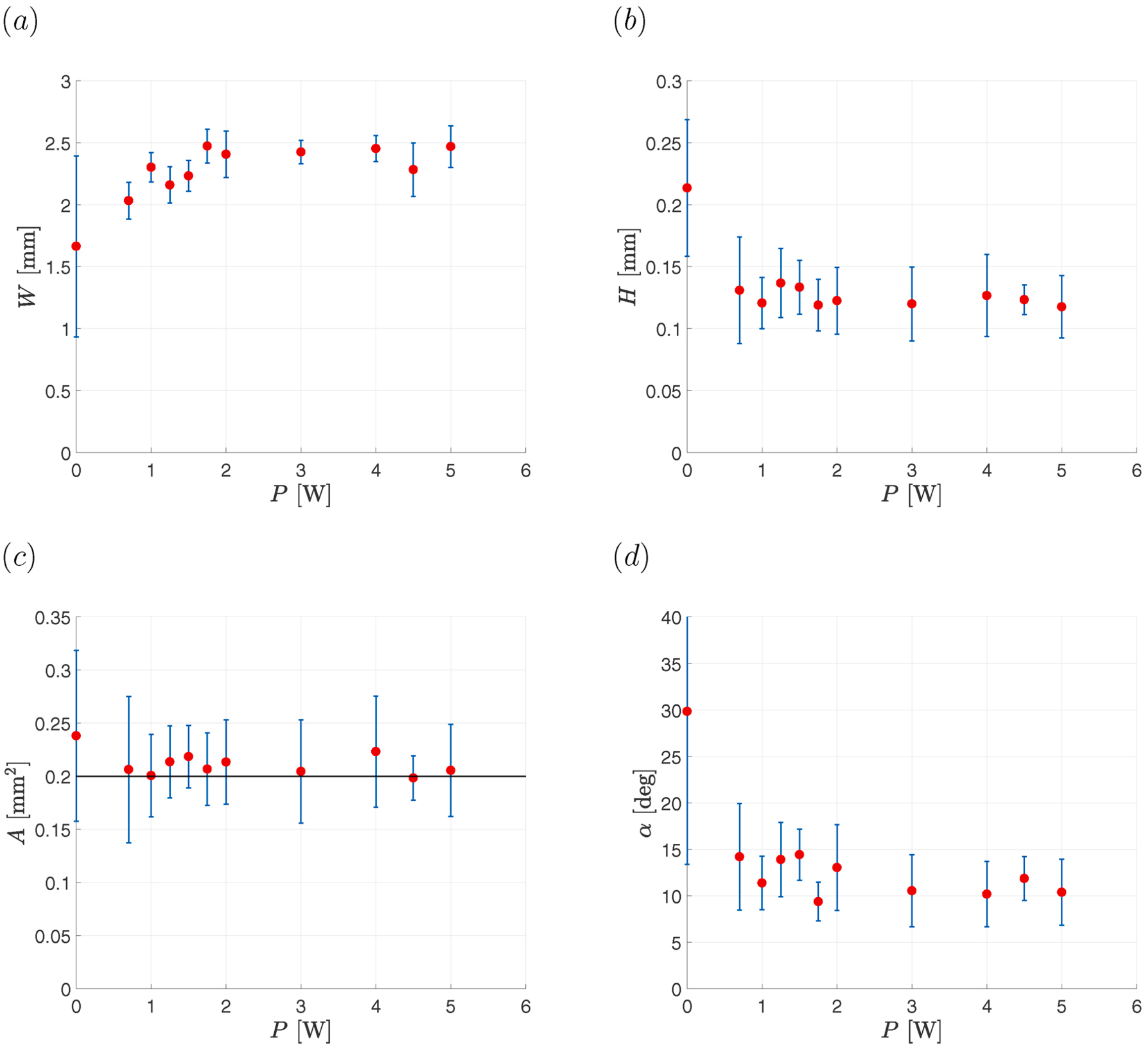

Fig. 4. Solder line (a) width, (b) height, (c) cross-sectional area, and (d) contact angle against power for fixed tip height 0.2 mm, tip speed 180 mm/min, and target cross-sectional area 0.2 mm^2. Error bars are 95% confidence intervals.

the relatively large error bars increase with tip height, which could be used to optimize the UAS process, e.g. a smaller tip height should be selected to reduce variability in the solder line. Lastly, a large increase in contact angle is observed for the largest tip height, consistent with reduced acoustic radiation pressure and a corresponding decrease in the work of adhesion (Fig. 5(d)).

Overall, the experimental results support the initial assumptions that higher power levels and lower tip heights increase the wettability of the solder line, i.e. increased width and decreased height and contact angle. This has been quantified and will help improve precision and repeatability in the UAS manufacturing process. Furthermore, these experiments confirm that the automated UAS system used for this study can repeatably produce solder lines with constant cross sectional area.

4. Theoretical model

It is clear from experimental observation that acoustic radiation pressure leads to enhanced wetting, as shown in Fig. 1. The goal of this section is to derive a physical-based model that can predict the solder line geometry from the UAS process to compare with experiment. It is worth noting the length scale of a typical solder line in experiment has a half-width or radius $L \approx 1.2$ mm. For reference, the capillary length is given by $\ell_c \equiv \sqrt{\sigma/\rho g}$, where σ is the surface tension, ρ is the density, and g is the gravitational force. For Sn-Bi based solder $\ell_c \approx 2.2$ mm [42,43]. Since $L < \ell_c$ it is assumed that surface tension forces dominate gravitational forces. The time scale associated with the tip frequency 60 kHz is smaller than the capillary $t_c \equiv \sqrt{\rho L^3/\sigma} = 0.006$ s time scale, such that the interface evolves quasi-statically. Otherwise stated, the interface shape adapts instantaneously to the acoustic radiation pressure such that the static interface shape will be the focus of this study.

4.1. Young-Laplace equation

Capillary shapes are described by the Young-Laplace equation,

$$\Delta p = \sigma(\kappa_1 + \kappa_2), \tag{2}$$

which relates the pressure difference Δp across the interface to the sum of principal curvatures κ_1, κ_2 there [42,44]. In this study, the solder line is immersed in a passive gas and the sources of pressure p within the solder bead are the hydrostatic and acoustic radiation pressures. The interface shape $z = z(x)$ is defined in a Cartesian coordinate system $x - z$, as shown in Fig. 6. This yields the following shape equation

$$p = \sigma \frac{\frac{\partial^2 z}{\partial x^2}}{\left(1 + \left(\frac{\partial z}{\partial x}\right)^2\right)^{3/2}}, \tag{3}$$

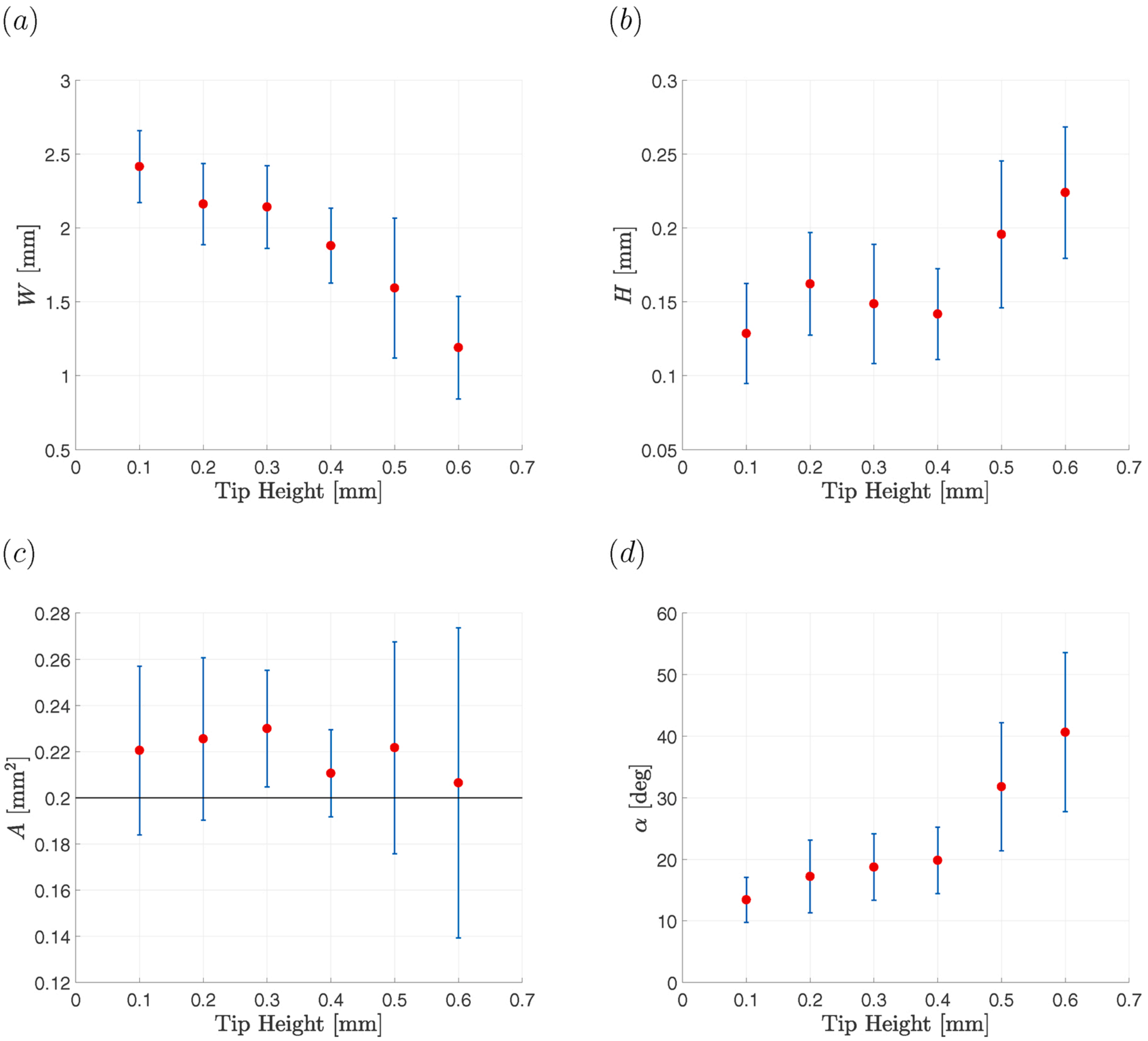

Fig. 5. Solder line (a) width, (b) height, (c) cross-sectional area, and (d) contact angle against the tip height for fixed power 4.5 W, tip speed 180 mm/min, and target cross-sectional area $A = 0.2\,\text{mm}^2$. Error bars are 95% confidence intervals.

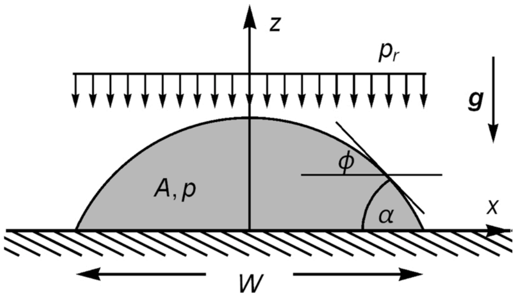

Fig. 6. Definition sketch of solder line cross-sectional shape.

which is a second-order, nonlinear differential equation [45].

The pressure appears linearly in the Navier-Stokes equations and accordingly we can sum the individual pressures associated with the forces acting on the solder line can be summed into Eq. (3). These include the unknown Laplace pressure p needed to enforce volume conservation, the hydrostatic pressure due to gravity,

$$p_h = \rho g\ z, \tag{4}$$

and the acoustic radiation pressure from the soldering tip, which will be discussed in detail [46–50]. The acoustic radiation tensor describes the stresses on the surface of an obstacle in an acoustic field [51]. The term acoustic radiation pressure has been adopted to refer to the time-averaged stress acting on the surface of the obstacle and the radiation force is the resultant time-averaged force due to the radiation pressure [52]. For this study, the radiation force can be projected onto the direction normal to the interface to obtain an equation for the acoustic radiation pressure [53].

To derive an expression for the acoustic radiation pressure applied to the solder line interface, we consider a wave velocity due to an acoustic source, $\boldsymbol{u} = \omega\xi_o cos\left(\frac{2\pi z}{\lambda} - \omega t\right)$, where ω is the angular frequency of oscillations, and ξ_0 is the amplitude of vibrations [54]. Substituting this form into the Navier-Stokes equations and taking the time average of each term delivers an expression for the acoustic radiation pressure

$$p_r = \frac{\rho(\omega\xi_0)^2}{2}\left(\frac{B}{2C} + cos^2(\phi)\right), \tag{5}$$

where the constant B/C is known as the parameter of nonlinearity in fluids [55]. The geometric factor $\cos\phi$ is related to the tangent angle ϕ to the interface and can be expressed as $cos\phi = x/\sqrt{x^2 + z^2}$. A term including the nonlinearity parameter $B/2C$ can be absorbed into the constant Laplace pressure p and is dropped for simplicity. The acoustic radiation pressure p_r can then be written as

$$p_r = \frac{\rho(\omega\xi_0)^2}{2}\left(\frac{x^2}{x^2+z^2}\right) \tag{6}$$

Combining the three pressure terms p, p_h, p_r into the Young-Laplace equation yields the following governing equation for the solder line shape,

$$p + \rho g z + \frac{\rho(\omega\xi_0)^2}{2}\left(\frac{x^2}{x^2+z^2}\right) = \sigma\frac{\frac{\partial^2 z}{\partial x^2}}{\left(1+\left(\frac{\partial z}{\partial x}\right)^2\right)^{3/2}}. \tag{7}$$

4.2. Boundary and integral conditions

Eq. (7) is supplemented by a set of boundary and integral conditions needed to specify the interface shape. Incompressibility requires that cross-sectional area A is conserved, which can be expressed as the following integral condition,

$$\int_0^R z(x)\mathrm{dx} = A. \tag{8}$$

For reference, $A = 0.2\,\mathrm{mm}^2$ in this study. At the axis-of-symmetry $x = 0$, we enforce

$$\frac{\mathrm{dz}}{\mathrm{dx}} = 0|_{x=0}, \tag{9}$$

and at the contact line $x = R$, a contact condition is applied

$$z = 0|_{x=R}. \tag{10}$$

The boundary conditions (9) and (10) and integral condition (8) are combined with Eq. (7) to form a well-posed system that can be solved for the interface shape $z(x)$ and unknown pressure p.

4.3. Non-dimensionalization

The governing equations are non-dimensionalized by scaling lengths with the radius of the cross-section of the solder line R and pressures with the capillary pressure σ/R [53]:

$$\hat{x} = \frac{x}{R}, \quad \hat{z} = \frac{z}{R}, \quad \hat{p} = \frac{R}{\sigma}p.$$

Here hats denote dimensionless quantities. Applying this scaling to Eq. (7) yields

$$\hat{p} + \mathrm{Bo}\hat{z} + \frac{1}{2}\mathrm{We}\left(\frac{\hat{x}}{\sqrt{\hat{x}^2+\hat{z}^2}}\right) = \frac{d^2\hat{z}/d\hat{x}^2}{\left(1+(d\hat{z}/d\hat{x})^2\right)^{3/2}}, \tag{11}$$

where the Bond number $\mathrm{Bo} \equiv \rho g R^2/\sigma$ and Weber number $\mathrm{We} = \rho\omega\xi_0^2 R/\sigma$. Similarly, the boundary and integral conditions (8)–(10) can be written as

$$\frac{d\hat{z}}{d\hat{x}} = 0\ |_{x=0}, \quad \hat{z} = 0\ |_{x=1}, \quad \int_0^1 \hat{z}(\hat{x})d\hat{x} = \hat{A}. \tag{12}$$

We now drop the hats for simplicity.

4.4. Numerical solution

Eqs. (11) and (12) define a well-posed boundary value problem for the solder line shape that can be solved numerically using the MATLAB built-in function bvp4c. To satisfy the integral condition, we introduce a new variable for the area A that can be defined through the relationship

$$\frac{\mathrm{d}A}{\mathrm{dx}} = z \tag{13}$$

which is recognized as the differential form of the integral condition. The associated boundary conditions are given by

$$A(0) = 0, \quad A(1) = \hat{A}, \tag{14}$$

and by construction, each solution will enclose a non-dimensional area $\hat{A}$. To summarize, for a given set of parameters Bo, We, $\hat{A}$ the numerical solution will deliver the interface shape $z(x)$, contact-angle α, and pressure p.

4.5. Results

We are particularly interested in the contact-angle α which appears in the work of adhesion, Eq. (1), and describes the chemical bond between solder and substrate in this application. Fig. 7(a) plots the contact-angle α against area $\hat{A}$, as it depends upon Weber number (We). For fixed We, it can be seen that α increases with $\hat{A}$, as is expected. For fixed contact-angle α, increasing We leads to a decrease in $\hat{A}$. A decreasing non-dimensional area corresponds to an increased wetted width because the area is scaled by and is inversely proportional to the true radius squared, $\hat{A} = A/R^2$. Therefore, higher Weber numbers lead to increased wetted widths, which will be discussed in detail shortly. This is best seen

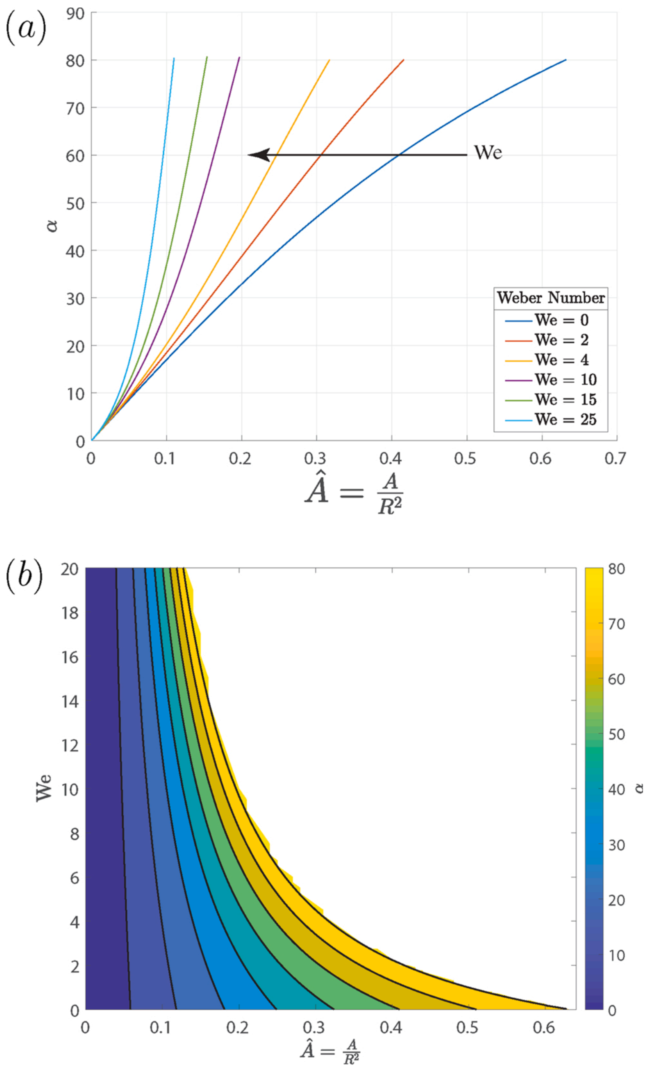

Fig. 7. Contact angle α against (a) area $\hat{A}$ as it depends upon Weber number (We), and (b) against Weber number (We) and area $\hat{A}$, for $\mathrm{Bo} = 0$.

in Fig. 7(b) which plots We against $\widehat{A}$ as it depends upon α. For fixed wetting conditions α, Fig. 7(b) shows how to choose We to achieve a given $\widehat{A}$. This information could be useful in UAS applications where precision soldering is desired.

Fig. 1 clearly shows an increase in wetted width with ultrasonication and we show that our model yields corresponding predictions. To begin, recall that lengths were scaled such that the wetted width was fixed and the contact-angle was allowed to vary. We note that a complementary boundary condition is one where the contact-angle α is fixed and the wetted width is allowed to vary [37,56,57]. This condition is appropriate for the UAS process and we show how to interpret our results accordingly. For fixed α and We, the non-dimensional area $\widehat{A} = A/R^2$ and dimensional area A define the length scale $R = \sqrt{A/\widehat{A}}$. For reference, $A = 0.2\,\text{mm}^2$ in the experiments. Our predicted capillary shapes can be unscaled with this R, as shown in Fig. 8. Fig. 8(a) shows two scaled shapes with fixed angle $\alpha = 50^\circ$ but different $\widehat{A}$, whereas Fig. 8(b) shows the unscaled shapes with identical α and A, but dramatically different wetted widths. This is consistent with our experimental observations in which increased ultrasonic power leads to increased wetting.

5. Comparison with experiment

The acoustic radiation pressure applied to the solder line is an unknown quantity, but it is related to the ultrasonic power delivered to the solder tip in our automated UAS system. This makes quantitative comparison between theory and experiment challenging. Our approach will be to introduce an empirical scale factor in order to establish a relationship between the ultrasonic power to the acoustic Weber number. This relationship can then be used to predict wetted widths to be compared with experimental observations.

To begin, we observe note that the Weber number (We) is related to the amplitude of tip vibration. A digital micrometer was used to measure the amplitude of the solder tip displacement as a function of ultrasonic power, as shown in Table 1. The Weber number is directly proportional to the amplitude squared ξ_0^2, i.e., doubling the amplitude increases the Weber number by a factor of four. Therefore, the output power level from the Sunbonder control box can be related to the acoustic radiation pressure applied to the solder line through the Weber number by a to-be-determined scale factor. The empirical scale factor can be found by dividing the true width from experiments by the scaled width from the model $s = (\text{truewidth})/(\text{modelwidth})$. We choose our normalization by making the width at We = 20 (4.216 mm) equal to the experimental width at a power level of 4 W (2.45 mm). This gives a scaling factor $s = 0.5811$ with corresponding widths and heights, as they depend upon We, given in Table 2. These predicted widths more accurately reflect those shown in experiment.

Table 1
Solder tip amplitude at different power levels with Weber number (We) multiplier.

Power [W]	Amplitude [μm]	We multiplier
0.7	1	1
1	1.2	1.44
1.5	1.35	1.82
2	1.5	2.25
3	1.6	2.56
4	1.75	3.06
5	1.85	3.42
6	2	4

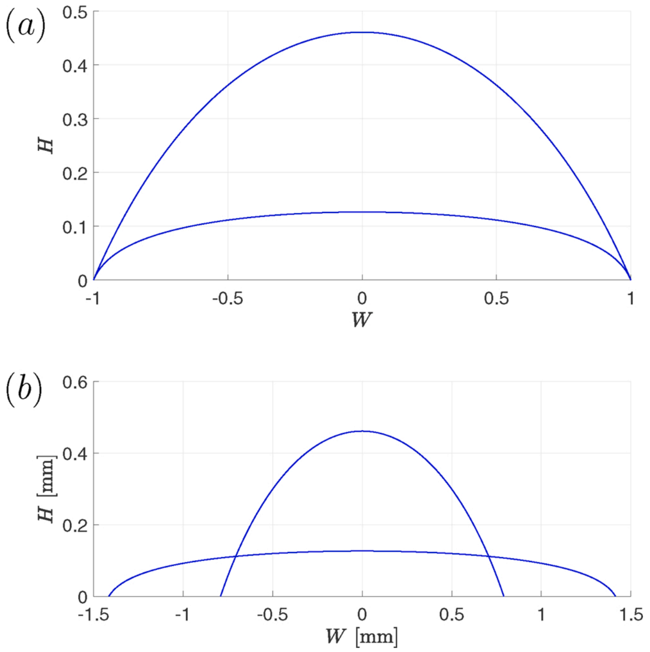

Fig. 8. Predicted capillary shapes illustrating the We number effect by plotting the (a) scaled and (b) unscaled shapes for We=0 and We=20 with $\alpha = 50^\circ$.

Table 1 can be used to relate the Weber number to a given power level. Recall that the width at We = 20 has been chosen to match the width of a line soldered at 4 W. Therefore, it can be concluded from Table 1 that the Weber number at 4 W will be 3.06 times greater than the Weber number at 0.7 W. This reasoning applies to every power level, as shown in Table 3. The width corresponding to each Weber number is taken from Table 2 and compared to the average width at each power level measured from experiment. The percent error between the experimental and model widths is also listed in Table 3. The quantitative comparison between model and experiment has been achieved over a wide range of power values. It should be noted that percent error between the experimental and theoretical heights do not match up as well as the widths due to a geometric effect imposed by the soldering tip. Nevertheless, the confidence in comparison between model and experiment for the width suggest that the wetted width of a solder line in the UAS process can be accurately predicted a priori. This is critically important for precision soldering using our automated manufacturing process.

6. Concluding remarks

We have studied the wetting properties of solder-to-glass in the UAS process from both an experimental and theoretical perspective. Our focus was to understand how acoustic radiation pressure from the

Table 2
Scaled width and height at each Weber number for $\alpha = 12^\circ$ and $A = 0.2\,\text{mm}^2$.

We	Width [mm]	Height [mm]
0	1.964	0.1029
1	1.993	0.1008
2	2.016	0.0990
3	2.039	0.0973
4	2.071	0.0953
5	2.096	0.0936
6	2.122	0.0920
7	2.158	0.0901
8	2.177	0.0889
9	2.196	0.0877
10	2.206	0.0869
12	2.279	0.0836
15	2.348	0.0803
17	2.385	0.0786
20	2.450	0.0759
22	2.492	0.0742
25	2.551	0.0720

Table 3
Comparison between wetted width predicted by the theoretical model and measured in experiment.

Power [W]	We	Model width	Exp. width	% Error
0.7	6	2.122	2.032	4.43
1	9	2.196	2.301	4.56
1.5	12	2.279	2.232	2.12
2	15	2.348	2.406	2.43
3	17	2.385	2.425	1.64
4	20	2.450	2.452	0.08
5	22	2.492	2.469	0.94

ultrasonic solder tip vibrations affects the solder bead geometry. Systematic experiments were conducted to investigate the role of (i) ultrasonic power and (ii) solder tip height using our automated UAS system which has precision control over a large number of experimental parameters. Our experiments show that wettability increases (increased wetted width and decreased contact angle) with (i) increasing ultrasonic power and (ii) decreasing tip height, both of which lead to increased acoustic radiation pressure. These results allow us to optimize our system for wettability with minimal ultrasonic power, which often leads to undesired heating of the PZT transducer that can cause thermal drift in the acoustic power delivered to the solder melt. Furthermore, we have developed a theoretical model for the cross-sectional geometry of the solder line using the capillary shape equation with acoustic radiation pressure included. The numerical results to our model agree well with our experimental observations, which suggests we are able to accurately predicted the wetting properties of the solder lines laid down by our UAS system. This is important for implementation of an automated UAS system in a precision manufacturing process.

Enhanced wettability due to UAS is often associated with enhanced adhesion strength of the solder bond, as described by the work of adhesion (1). Our work clearly shows that one should expect enhanced adhesion in UAS, but this has yet to be quantified and should be pursued further in future work to test the mechanical strength of the solder-to-glass bond. This could include tension, lap shear, or peel-off tests. In addition, the role of material chemistry should be explored to better understand the role rare earth elements in the solder composition play with regards to the chemical bond at the metal-to-glass interface. These combined should give a clear understanding of the physics of wetting and adhesion in the complex multiphysics UAS process.

Declaration of Competing Interest

The authors report no declarations of interest.

Acknowledgements

We would like to acknowledge the support of L3Harris and the NSF-INTERN program for a supplement to NSF GrantCBET-1750208. We would also like to thank Jennifer Brown, Peter Tilton, and Hyrel 3D for their technical assistance.

References

[1] Gao F, Rajathurai K, Cui Q, Zhou G, NkengforAcha I, Gu Z. Effect of surface oxide on the melting behavior of lead-free solder nanowires and nanorods. Appl Surf Sci 2012;258(19):7507–14.

[2] Zhang L, Sun G, Li L, Shang JK. Effect of copper oxide layer on solder wetting temperature under a reduced atmosphere. In: 2007 8th International Conference on Electronic Packaging Technology; 2007. p. 1–4.

[3] Graff K. Macrosonics in industry: ultrasonic soldering. Ultrasonics 1977;15(2): 75–81.

[4] Zado FM. Soldering flux. US Patent 4,168,996; 25 September 1979).

[5] Courtney D. Health hazards of soft soldering in the electronics industry. Rev Environ Health 1985;5(1):1–26.

[6] Fawcett I, Taylor A, Pepys J. Asthma due to inhaled chemical agents – fumes from 'Multicore' soldering flux and colophony resin. Clin Allergy 1976;6(6):577–85.

[7] Pepys J, Pickering C. Asthma due to inhaled chemical fumes-amino-ethyl ethanolamine in aluminium soldering flux. Clin Exp Allergy 1972;2(2):197–204.

[8] Arita K, Nishimura T. Soldering flux. US Patent 5,417,771; 23 May 1995.

[9] Chang-Chien Y-C, Song J-M, Huang B-C, Chen W-T, Shie C-R, Hsu C-Y. Oxidation properties of Sn-Cu-Ni solders with minor alloying additions. In: 2010 5th international microsystems packaging assembly and circuits technology conference; 2010. p. 1–4.

[10] Vianco PT. Corrosion issues in solder joint design and service. 1999. https://www.osti.gov/servlets/purl/14961.

[11] Antonevich J. Fundamentals of ultrasonic soldering. Weld J 1976;55(7):200s–7s.

[12] Lanin VL. Ultrasonic soldering in electronics. Ultrason Sonochem 2001;8(4): 379–85. https://doi.org/10.1016/S1350-4177(01)00065-7.

[13] Yonekura D, Ueki T, Tokiyasu K, Kira S, Wakabayashi T. Bonding mechanism of lead-free solder and glass plate by ultrasonic assisted soldering method. Mater Des (1980–2015) 2015;65:907–13.

[14] Franc J-P. The Rayleigh-Plesset equation: a simple and powerful tool to understand various aspects of cavitation. Fluid dynamics of cavitation and cavitating turbopumps. Springer; 2007. p. 1–41.

[15] Suslick KS, Price GJ. Applications of ultrasound to materials chemistry. Annu Rev Mater Sci 1999;29(1):295–326.

[16] Li Z, Xu Z, Ma L, Wang S, Liu X, Yan J. Cavitation at filler metal/substrate interface during ultrasonic-assisted soldering. Part I: cavitation characteristics. Ultrason Sonochem 2018;49:249–59.

[17] Li Z, Xu Z, Ma L, Wang S, Liu X, Yan J. Cavitation at filler metal/substrate interface during ultrasonic-assisted soldering. Part II: cavitation erosion effect. Ultrason Sonochem 2019;50:278–88. https://doi.org/10.1016/j.ultsonch.2018.09.027.

[18] Hashemabad SG, Gu Z, Ando T. Flux-less direct soldering of aluminum by ultrasonic surface activation. J Mater Process Technol 2016;233:135–41. https://doi.org/10.1016/j.jmatprotec.2016.02.015.

[19] Kolenák R, Šebo P, Provazník M, Koleňáková M, Ulrich K. Shear strength and wettability of active Sn3.5Ag4Ti(Ce,Ga) solder on Al_2O_3 ceramics. Mater Des 2011; 32(7):3997–4003. https://doi.org/10.1016/j.matdes.2011.03.022.

[20] Lanin V. Ultrasonic soldering in electronics: new opportunities. In: Willard TG, editor. Solid state electrochemistry. Nova Science Publishers, Inc.; 2010. p. 201–11. https://doi.org/10.1227/01.NEU.0000313112.49285.47 [Ch. 6].

[21] Mustafa MY, Hilmy I, Adesta E. Effect of surface roughness on adhesion strength in ultrasonic soldering of glass. ARPN J Eng Appl Sci 2015;10(21):9736–43.

[22] Yonekura D, Ueki T, Taguchi Y. Application of ultrasonic assisted soldering method to hard-to-solder material. Int J Mod Phys B 2018;32(19):1840054. https://doi.org/10.1142/S0217979218400544.

[23] Faridi HR. Flux-free ultrasonic soldering of aluminum and stainless steel [Ph.D. thesis]. Oregan Graduate Institute of Science and Technology; 2000. https://doi.org/10.6083/M44T6GNX.

[24] Kolenák R, Prach M, Kostolný I. Ultrasonic soldering of Cu and Al_2O_3 ceramics by use of Bi-La and Bi-Ag-La solders. Acta Polytech 2016;56(2):126–31. https://doi.org/10.14311/AP.2016.56.0126.

[25] Kolenak R, Kostolny I, Drápala J, Drienovsky M, Sahul M. Research on joining metal-ceramics composite Al/Al_2O_3 with Cu substrate using solder type Zn-In-Mg. J Compos Mater 2019;53(10):1411–22. https://doi.org/10.1177/0021998319835304.

[26] Luft W, Maiden EE. Temperature cycling effects on solar panels. IEEE Trans Aerosp Electron Syst 1969;(6):943–50.

[27] Tsuzuki K, Inoue K, Takada T, Takeyama Y. Photovoltaic device and manufacturing method of the same. US Patent 5,667,596; 16 September 1997.

[28] Jones J, Thomas J. Ultrasonic soldering of aluminum. In: Symposium on solder; 1957.

[29] Terrill JR, Dzierski SF. Fluxless ultrasonic soldering of aluminum tubes. US Patent 3,680,200; 1 August 1972.

[30] Kim J, Chiao M, Lin L. Ultrasonic bonding of In/Au and Al/Al for hermetic sealing of MEMS packaging. In: Technical digest. MEMS 2002 IEEE international conference. Fifteenth IEEE international conference on micro electro mechanical systems (Cat. No. 02CH37266); 2002. p. 415–8.

[31] Kang SK, Choi WK, Yim MJ, Shih DY. Studies of the mechanical and electrical properties of lead-free solder joints. J Electron Mater 2002;31(11):1292–303. https://doi.org/10.1007/s11664-002-0023-9.

[32] Gaboreau S, Vieillard P. Prediction of Gibbs free energies of formation of minerals of the alunite supergroup. Geochim Cosmochim Acta 2004;68(16):3307–16.

[33] Shacklette LW, Gerrity DL, Lange MR, Beachboard JC, Smith R. Interfacial studies of a metallurgical bond between "activated" ultrasonically applied solder and high purity fused silica. In: Material technologies and applications to optics, structures, components, and sub-systems III, vol. 10372; 2017. p. 1037207.

[34] Shaffer J, Maassen K, Wilson C, Tilton P, Thompson L, Choi H, et al. Development of an open-sourced automated ultrasonic-assisted soldering system. J Manuf Process 2019;47:284–90.

[35] Sangiorgi R, Muolo ML, Chatain D, Eustathopoulo N. Wettability and work of adhesion of nonreactive liquid metals on silica. J Am Ceram Soc 1988;71(9):742–8.

[36] Ebnesajjad S, Landrock AH. Adhesives technology handbook. William Andrew; 2014.

[37] Bostwick J, Steen P. Liquid-bridge shape stability by energy bounding. IMA J Appl Math 2015;80(6):1759–75.

[38] Leighton T. The acoustic bubble. Academic Press; 2012.

[39] Maassen KF, Brown JS, Choi H, Thompson LL, Bostwick JB. Acoustic analysis of ultrasonic assisted soldering for enhanced adhesion. Ultrasonics 2020;101:106003.

[40] Bostwick J, Steen P. Stability of constrained cylindrical interfaces and the torus lift of plateau-Rayleigh. J Fluid Mech 2010;647:201–19.

[41] Bostwick J, Steen P. Static rivulet instabilities: varicose and sinuous modes. J Fluid Mech 2018;837:819–38.

[42] De Gennes P-G, Brochard-Wyart F, Quéré D. Capillarity and wetting phenomena: drops, bubbles, pearls, waves. Springer Science & Business Media; 2013.

[43] Moser Z, Gasior W, Debski A. Database of Pb-free soldering materials, surface tension and density, experiment vs. modeling. Data Sci J 2005;4:195–208.

[44] Rotenberg Y, Boruvka L, Neumann A. Determination of surface tension and contact angle from the shapes of axisymmetric fluid interfaces. J Colloid Interface Sci 1983; 93(1):169–83.

[45] Langbein DW. Capillary surfaces: shape-stability-dynamics, in particular under weightlessness, vol. 178. Springer Science & Business Media; 2002.

[46] Beyer RT. Radiation pressure-the history of a mislabeled tensor. J Acoust Soc Am 1978;63(4):1025–30.

[47] Biwersi S, Manceau J, Bastien F. Displacement of droplets and deformation of thin liquid layers using flexural vibrations of structures. influence of acoustic radiation pressure. J Acoust Soc Am 2000;107(1):661–4.

[48] Cinbis C, Mansour N, Khuri-Yakub B. Effect of surface tension on the acoustic radiation pressure-induced motion of the water-air interface. J Acoust Soc Am 1993;94(4):2365–72.

[49] Chu B-T, Apfel RE. Acoustic radiation pressure produced by a beam of sound. J Acoust Soc Am 1982;72(6):1673–87.

[50] Lee C, Wang T. Acoustic radiation pressure. J Acoust Soc Am 1993;94(2): 1099–109.

[51] Brillouin L. Les tenseurs en mécanique et en élasticité. 1949.

[52] Hasegawa T, Kido T, Iizuka T, Matsuoka C. A general theory of Rayleigh and Langevin radiation pressures. Acoust Sci Technol 2000;21(3):145–52.

[53] Manor O, Dentry M, Friend JR, Yeo LY. Substrate dependent drop deformation and wetting under high frequency vibration. Soft Matter 2011;7(18):7976–9.

[54] Morse PM, Ingard KU. Theoretical acoustics. Princeton University Press; 1986.

[55] Beyer RT. Parameter of nonlinearity in fluids. J Acoust Soc Am 1960;32(6):719–21.

[56] Bostwick J, Steen P. Stability of constrained capillary surfaces. Annu Rev Fluid Mech 2015;47:539–68.

[57] Michael D, Williams P. The equilibrium and stability of sessile drops. Proc R Soc Lond A: Math Phys Sci 1977;354(1676):127–36.